



## Discharge Model for LiFePO<sub>4</sub> Accounting for the Solid Solution Range

Uday S. Kasavajjula,<sup>a</sup> Chunsheng Wang,<sup>b,\*</sup> and Pedro E. Arce<sup>a</sup>

<sup>a</sup>Department of Chemical Engineering, Tennessee Technological University, Cookeville, Tennessee 38501, USA

<sup>b</sup>Department of Chemical & Biomolecular Engineering, University of Maryland, College Park, Maryland 20742, USA

A comprehensive discharge model for LiFePO<sub>4</sub> electrode, including Li-ion diffusion in both the alpha and the beta solid solution phases, and phase transformation was developed. For the discharge model, the phase transformation, driven by the interfacial lithium concentration differences in both alpha and beta phases, was considered to be strongly dependent on the type of interface formed between the alpha and beta phases (coherent, semicoherent, and incoherent). By using the model as a tool, effects of extending the alpha and the beta solid solutions and reducing the particle size of LiFePO<sub>4</sub> on rate performance of LiFePO<sub>4</sub> were analyzed. The model developed in this article is applicable for predicting the discharge behavior of any other electrodes with phase transformation.

© 2008 The Electrochemical Society. [DOI: 10.1149/1.2980420] All rights reserved.

Manuscript submitted March 27, 2008; revised manuscript received July 23, 2008. Published September 25, 2008.

The rate capability of LiFePO<sub>4</sub> is a critical issue for the commercialization of Li-ion batteries in hybrid electric vehicles and battery electric vehicles. Low electronic conductivity ( $10^{-9}$ – $10^{-10}$  S/cm),<sup>1–3</sup> poor Li ion diffusivity,<sup>4</sup> and sluggish phase transformation between the Li-deficient phase (Li<sub>1-x</sub>FePO<sub>4</sub>,  $x \sim 0.05$ ) and Li-rich phase (Li<sub>1+y</sub>FePO<sub>4</sub>,  $y = 0.78$ – $0.95$ )<sup>5</sup> were some of the key reasons for its poor rate capability. Though several methods<sup>6–9</sup> have been proven to enhance the rate performance of LiFePO<sub>4</sub> cathodes, the exact mechanism to improve the rate capability is still unclear. The high-rate performance of supervalent cation-doped LiFePO<sub>4</sub> has been initially attributed to the improved electronic conductivity.<sup>5</sup> However, it was recently found that the high-rate capability of doped LiFePO<sub>4</sub> is also affected by the fast rate of phase transformation. This is due to the formation of a strained coherent interface, which increases the solid solution range.<sup>10</sup> The critical role of the solid solution range in improving the rate performance is also evident from the high-rate performance of Mn<sup>2+</sup>-doped LiFePO<sub>4</sub><sup>12,13</sup> and nanosize LiFePO<sub>4</sub>.<sup>11</sup> Both reduction of the particle size<sup>11</sup> and the partial substitution of Fe in LiFePO<sub>4</sub> by Mn<sup>2+</sup><sup>12,13</sup> were also found to increase the solid solution range. Although these results demonstrate the importance of the solid solution range, the particle size, and the phase transformation rate in increasing the rate performance of LiFePO<sub>4</sub> electrodes, the actual reasons behind the improvement of the rate capability are not clearly known.

A systematic study on the influence of these factors on rate performance of LiFePO<sub>4</sub> is critical for attaining further improvement in the rate capability, and it can be performed by developing a mathematical model. It is well known that LiFePO<sub>4</sub> is an electrode material undergoing phase transformation during charge/discharge, and that lithium-ion transport in LiFePO<sub>4</sub> takes place by a three-step mechanism: (i) Diffusion of Li<sup>+</sup> ion in Li-rich (β) phase, (ii) transfer of Li<sup>+</sup> ion across the α/β phase boundary (phase transformation), and (iii) diffusion of Li<sup>+</sup> ion in Li-deficient (α) phase. The phase transformation in LiFePO<sub>4</sub> during the charge/discharge process is generally driven by the differences between the real concentration and the equilibrium concentration in α and β phases at the interface. Also, the rate of phase transformation depends on the interface mobility and the Li-ion diffusivity in the α and β phases. If the interface mobility is much faster than the lithium-ion diffusion in α and β phases, then the phase transformation will be controlled by the Li ion diffusion (diffusion controlled); otherwise, it is controlled by the interface mobility (interface controlled). If the interface mobility is comparable to lithium-ion diffusivity, the phase transformation will

be controlled by both the interface mobility and the lithium-ion diffusion (mixed controlled).

The discharge behavior of phase transformation electrodes in Li-ion battery is well described by three different mathematical models;<sup>14–16</sup> they differ in the way the Li<sup>+</sup>-ion transport process is modeled. The model developed in Ref. 14 considers only the lithium-ion diffusion in the β phase. It also assumes that the interface mobility (Li<sup>+</sup> ion transfer across the phase boundary) is very fast, and the discharge process is controlled by the lithium-ion diffusion in the β phase. The model developed in Ref. 15 includes lithium-ion diffusion in both α and β phases, but it assumes a fast Li<sup>+</sup>-ion transfer across the phase boundary. The model developed by Wang et al.<sup>16</sup> represents a more general case, because it assumes that the phase transformation is controlled by the lithium-ion diffusion in the β phase and the interface mobility. However, the lithium-ion diffusion in the α phase was not included to simplify the calculations.<sup>16</sup>

Due to the assumptions used in describing the lithium-ion transport process, the three models briefly described above were only able to predict the discharge behavior of certain phase transformation electrodes. For example, the models developed in Ref. 14 and 15 are applicable only to electrode materials whose discharge process is controlled by the lithium-ion diffusion. Due to the assumption of diffusion-controlled phase transformation (unlimited interface mobility), the effect of interface resistance (inversely proportional to the interface mobility) on the discharge rate capability cannot be simulated using these two models.<sup>14,15</sup> The model by Wang et al.<sup>16</sup> is applicable to electrode materials whose discharge process is controlled by either diffusion or interface or mixed diffusion and interface; in addition, the role of the β-phase diffusion coefficient and the interface mobility on discharge rate capability can be predicted. However, such a model cannot be used for analyzing the electrode materials with large α solid solutions, because it assumes that the lithium solubility in lithium-deficient (α) phase is negligible.

In the present work, a more comprehensive mathematical model is developed by modifying the model developed by Wang et al.<sup>16</sup> This is accomplished by considering the lithium-ion diffusion in Li-deficient (α) phase, and the phase transformation driving force induced from interfacial concentration difference in α phase. Here, the combination of models developed in Ref. 15 and 16 in their original form would not lead to a generalized model; this is because the model developed in Ref. 15 is applicable only for electrode materials with fast Li<sup>+</sup>-ion transfer across the phase boundary (very high interface mobility). Also, the models developed in Ref. 14–16 are the limiting cases of the generalized model developed in this article. As the lithium-ion diffusion in α phase was neglected in the

\* Electrochemical Society Active Member.

<sup>z</sup> E-mail: cswang@umd.edu

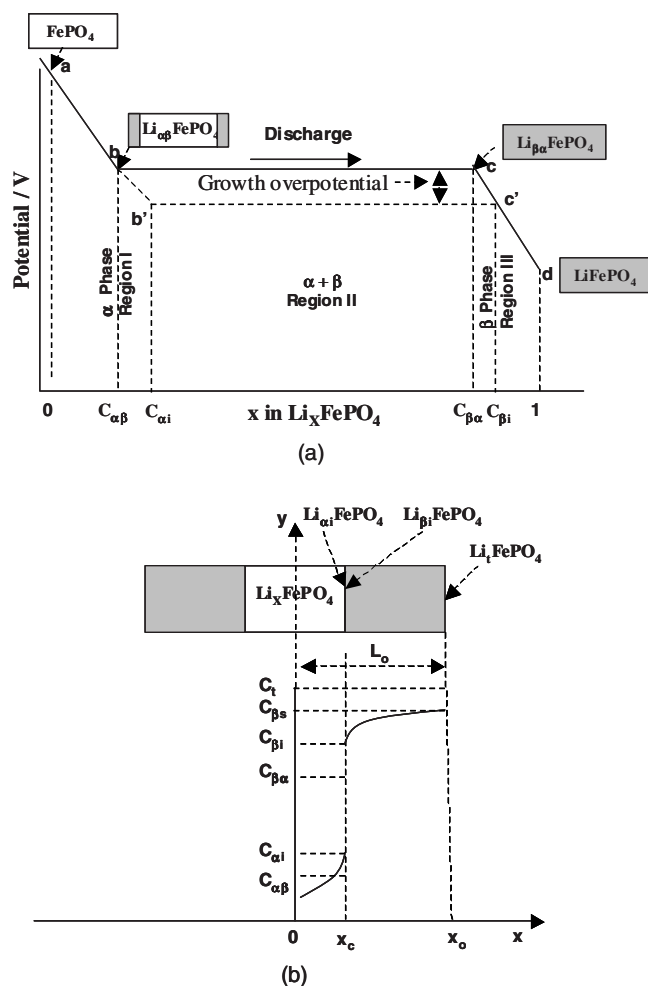


**Figure 1.** Schematic showing (a) phase transformation and (b) Li concentration distribution during the discharge of a  $\text{LiFePO}_4$  particle (Li insertion into  $\text{FePO}_4$ ).

model by Wang et al.,<sup>16</sup> the effects of  $\alpha$  solid solution range on the rate performance could not be determined. In the present article, by using this generalized model as a tool, the effects of solely extending the  $\alpha$  solid solution, simultaneously extending both the  $\alpha$  and the  $\beta$  solid solutions and reducing the particle size on rate capability, are studied.

### Model Development

The phase growth process during discharge of  $\text{LiFePO}_4$  described in the previous article by Wang et al.<sup>16</sup> is modified by considering the lithium-ion diffusion in the  $\alpha$  phase, the phase transformation driving force induced from the interface concentration difference in the  $\alpha$  phase, and the type of interface (coherence, semi-coherence, and incoherence). The discharge mechanism of  $\text{LiFePO}_4$  can be described as follows: At the beginning of the discharge process, Li inserts into surfaces of the electrode particle and diffuses into the interior of the particle. This process results in the formation of an  $\alpha$  solid solution, and the process continues until the Li content ( $x$ ) in  $\text{Li}_x\text{FePO}_4$  reaches the solid solubility limit ( $C_{\alpha\beta}$ ). This process corresponds to the initial potential sloping line in the discharge curve (a-b section in Fig. 1). Further insertion of Li into the lattice leads to the saturation of lithium in the solid solution phase ( $\text{Li}_x\text{FePO}_4$ ). When the lithium saturation level ( $x$ ) in the solid solution phase reaches  $C_{\alpha i}$ , a  $\beta$  phase with concentration of  $C_{\beta i}$  will be formed in the  $\alpha$  matrix, and as a result the value of discharge overpotential increases to the growth overpotential (b'-c' in Fig. 1). The

discharge overpotential is caused by a misfit strain energy resulting from the molar volume difference between  $\alpha$  and  $\beta$  phases. During further discharge, the  $\beta$  phase formed in the electrode near the boundary gradually increases in size, forming a continuous  $\beta$ -phase layer with a lithium concentration of  $C_{\beta i}$  ( $c'$  in Fig. 1) at the interface, which is higher than equilibrium concentration  $C_{\beta\alpha}$ . In addition to this, the interface concentration of the  $\alpha$  phase ( $C_{\alpha i}$ ) is also higher than the equilibrium concentration ( $C_{\alpha\beta}$ ). The growth of the  $\beta$  phase corresponds to the c'-d' section in Fig. 1. The relative difference  $[(C_{\beta i} - C_{\beta\alpha})/C_{\beta\alpha}, (C_{\alpha i} - C_{\alpha\beta})/C_{\alpha\beta}]$  between the real and equilibrium interface concentrations in  $\alpha$  and  $\beta$  phases will act as a driving force to overcome the energy barrier (misfit accommodation energy and interfacial energy) for phase growth. Further, lithium insertion will result in a growth of the  $\beta$  phase toward the center of the particle. Once the  $\alpha$  phase completely transforms into the  $\beta$  phase, subsequent lithium will start to dissolve into the  $\beta$  phase and form a solid solution with the lithium-ion concentration varying from  $C_{\beta i}$  to 1 (c'-d section in Fig. 1).

The lithium diffusion process in  $\text{LiFePO}_4$  during the discharge process can be modeled by modifying the transport equations proposed by Zhang et al.<sup>15</sup> based on the theory of mixed-mode phase transformations.<sup>17-20</sup> Because the discharge process is assumed to be controlled by a mixed-ion diffusion process and a phase transformation, the interfacial Li-rich phase concentration ( $C_{\beta i}$ ) and interfacial Li-deficient phase concentration ( $C_{\alpha i}$ ) will be different from the equilibrium concentrations  $C_{\beta\alpha}$  and  $C_{\alpha\beta}$  in region II (Fig. 1b). In addition, the transport equations reflect the use of Cartesian geometry instead of spherical geometry. The differential equations, initial condition, and boundary conditions of the governing model can be written as follows

Region I ( $0 \leq x \leq x_0$ )

$$\frac{\partial C_{\alpha}}{\partial t} = D_{\alpha} \left( \frac{\partial^2 C_{\alpha}}{\partial x^2} \right) \quad [1]$$

$$C_{\alpha} = 0 \quad t = 0 \quad [2]$$

$$D_{\alpha} \left( \frac{\partial C_{\alpha}}{\partial x} \right) = \frac{i}{F} \quad x = x_0 \quad [3]$$

$$\frac{\partial C_{\alpha}}{\partial x} = 0 \quad x = 0 \quad [4]$$

When the concentration at the particle surface ( $x = x_0$ ) reaches the maximum solubility of the initial solid solution  $\alpha$  phase ( $C_{\alpha\beta}$ ), the discharge process enters into the second region.

Region II

In  $\alpha$  phase [ $0 \leq x \leq x_c(t)$ ]

$$\frac{\partial C_{\alpha}}{\partial t} = D_{\alpha} \left( \frac{\partial^2 C_{\alpha}}{\partial x^2} \right) \quad [5]$$

$$\frac{\partial C_{\alpha}}{\partial x} = 0 \quad x = 0 \quad [6]$$

$$C_{\alpha} = C_{\alpha i} \quad x = x_c(t) \quad [7]$$

The initial condition for Eq. 5 is given by the lithium concentration profile inside the particle (in region I) taken when the surface concentration  $C_{\alpha}|_{x=x_0}$  reaches  $C_{\alpha\beta}$

In  $\beta$  phase [ $x_c(t) \leq x \leq x_0$ ]

$$\frac{\partial C_{\beta}}{\partial t} = D_{\beta} \left( \frac{\partial^2 C_{\beta}}{\partial x^2} \right) \quad [8]$$

$$C_{\beta} = C_{\beta\alpha} \quad t = 0 \quad [9]$$

$$D_{\beta} \left( \frac{\partial C_{\beta}}{\partial x} \right) = \frac{i}{F} \quad x = x_0 \quad [10]$$

$$C_{\beta} = C_{\beta i} \quad x = x_C(t) \quad [11]$$

The position of the interface [ $x_C(t)$ ] can be determined by performing a mass balance of lithium ions at the interface

$$\frac{dx_C(t)}{dt} = \frac{D_{\alpha} \left( \frac{\partial C_{\alpha}}{\partial x} \right)_{x=x_C(t)} - D_{\beta} \left( \frac{\partial C_{\beta}}{\partial x} \right)_{x=x_C(t)}}{(C_{\beta i} - C_{\alpha i})} \quad [12]$$

When the interface reaches the center of the particle [ $x_C(t) = 0$ ], i.e., when the particle is completely full of  $\beta$  phase, the discharge process enters into the third region.

Region III ( $0 \leq x \leq x_0$ )

$$\frac{\partial C_{\beta}}{\partial t} = D_{\beta} \left( \frac{\partial^2 C_{\beta}}{\partial x^2} \right) \quad [13]$$

$$D_{\beta} \left( \frac{\partial C_{\beta}}{\partial x} \right) = \frac{i}{F} \quad x = x_0 \quad [14]$$

$$\frac{\partial C_{\beta}}{\partial x} = 0, \quad x = 0 \quad [15]$$

The initial condition for Eq. 13 is given by the lithium concentration profile inside the  $\beta$  phase at the end of the region II.

To solve the system of equations in region II (Eq. 5-12), the interfacial concentration of the  $\beta$  and  $\alpha$  phases ( $C_{\beta i}$  and  $C_{\alpha i}$ ) needs to be determined. The Li-deficient phase concentration at the interface ( $C_{\alpha i}$ ) in Fig. 1 can be estimated by considering the driving force to be equal in both phases

$$\frac{C_{\alpha i} - C_{\alpha \beta}}{C_{\alpha \beta}} = \frac{C_{\beta i} - C_{\beta \alpha}}{C_{\beta \alpha}} \quad [16]$$

Equation 16 implies that the overpotential resulting from phase transformation kinetics is equal in both the phases (Fig. 1a).

The Li-rich phase concentration at the interface ( $C_{\beta i}$ ) is determined from the theory of mixed-mode phase transformations, which is given below.

**Theory of mixed-mode phase transformation.**—Generally, in a mixed-mode process, a steady-state condition exists across the interface leading to the balance of the flux of  $\text{Li}^+$  ion across the interface and towards the interface.<sup>21</sup>

The flux of  $\text{Li}^+$  ions across the interface<sup>21</sup> can be written as

$$J_{\text{Li}}^i = -M \times \Delta G_{\alpha-\beta}^i (C_{\beta i} - C_{\alpha i}) \quad [17]$$

where  $M$  is the interface mobility. This parameter depends on the degree of coherence of interface, buildup of stress, and deformations in the electrode material.  $C_{\beta i}$  is the actual concentration of the lithium-rich ( $\beta$ ) phase at the interface, which is higher than the local equilibrium concentration ( $C_{\beta \alpha}$ ) (Fig. 1b).  $C_{\alpha i}$  is the actual concentration of the lithium-deficient ( $\alpha$ ) phase at the interface, which is higher than the local equilibrium concentration ( $C_{\alpha \beta}$ ) (Fig. 1b);  $\Delta G_{\alpha-\beta}^i$  is the driving force for the occurrence of transformation from the  $\alpha$  to  $\beta$  phase. The driving force  $\Delta G_{\alpha-\beta}^i$  can be expressed in terms of free energy of the system as follows

$$\Delta G_{\alpha-\beta}^i = \Delta G_{\alpha-\beta}^{\text{chem}} - \Delta G_{\alpha-\beta}^{\text{elastic}} - \Delta G_{\alpha-\beta}^{\text{plastic}} - \Delta G_{\alpha-\beta}^{\text{surface}} \quad [18]$$

where  $\Delta G_{\alpha-\beta}^{\text{chem}}$  is the chemical free-energy difference resulting from the sum of deviations with respect to equilibrium concentration [ $(C_{\beta i} - C_{\beta \alpha})/C_{\beta \alpha} \cdot (C_{\alpha i} - C_{\alpha \beta})/C_{\alpha \beta}$ ].  $\Delta G_{\alpha-\beta}^{\text{surface}}$  is the free energy resulting from free surfaces, and it can be neglected when compared with other terms.  $\Delta G_{\alpha-\beta}^{\text{elastic}}$  and  $\Delta G_{\alpha-\beta}^{\text{plastic}}$  are the free energies resulting from the elastic and the plastic deformations, which are due to the volume change in forming the  $\beta$  phase. This change in volume

induces a lattice mismatch between the  $\alpha$  and  $\beta$  phases, and, depending on the lattice mismatch, the boundary between the lithiated and the delithiated phases can be considered as a coherent, semicoherent, or incoherent interface.<sup>10,21</sup> For the cases of coherent, semicoherent, and incoherent interfaces, the energy barrier for phase transformation is affected by elastic and plastic energies.<sup>24</sup> For the case of coherent interface, the elastic energy plays a major role in the total accommodation energy. Recently, Chiang et al.<sup>5,10,11</sup> reported that the energy barrier for phase transformation in nanoscale  $\text{LiFePO}_4$  (coherent interface) is mainly induced by the elastic energy ( $\Delta G_{\alpha-\beta}^{\text{elastic}}$ ). In their work, the calculated elastic energy increased with state of discharge and then decreased after reaching the peak at 50% state of discharge. This behavior is similar to the elastic energy change during hydrogen insertion into some metals.<sup>25</sup> However, for the semicoherent and incoherent interfaces, the plastic accommodation energy must be considered, because it has a more important role in the phase transformation than elastic energy.<sup>25</sup> Due to the striking similarity of phase transformation in hydrogen insertion into metal and in lithium insertion into  $\text{FePO}_4$ , and also due to the definite effect of total accommodation energy (not only elastic energy) on phase transformation kinetics,<sup>25</sup> data on the accommodation energy for hydrogen insertion into Nb,<sup>25</sup> and for temperature-induced austenite ( $\gamma$ )-ferrite ( $\alpha$ ) transformation in Fe-Mn alloys<sup>22</sup> were used to simulate the accommodation energy during Li insertion into  $\text{FePO}_4$ . Depending on the type of interface formed, the variation in accommodation energy during the phase transformation process is proposed to be described by the following expressions

$$\Delta G_{\alpha-\beta}^{\text{plastic}} + \Delta G_{\alpha-\beta}^{\text{elastic}} = A \times P \times \Delta G_{\alpha-\beta}^{\text{chem}} \times f[x_C(t)] \quad [19]$$

where

$$f[x_C(t)] = \sin[\pi x_C(t)] \quad \text{for coherent interface} \quad [20a]$$

$$f[x_C(t)] = 1 - x_C(t)^n \quad \text{for semicoherent and incoherent interface (Ref. 16)} \quad [20b]$$

The parameter “ $P$ ” in Eq. 19 is a proportionality factor that defines the peak value of accommodation energy. For example, if  $P$  is equal to 1, the accommodation energy will have a peak value equal to the chemical driving force. Because the magnitude of accommodation energy changes with the volume change,<sup>5</sup> the parameter “ $A$ ” in Eq. 19 was used as the accommodation energy factor to reflect the volume change. The value of  $A$  will decrease with the decrease in volume change of phase transformation. From Eq. 20a, for the case of a coherent interface, during the initial and final stages of the transformation [ $x_C(t) = 1, 0$ ], the accommodation energy is found to be zero and the accommodation energy is at its maximum at 50% of the transformation. From Eq. 20b, for the case of a semicoherent and incoherent interface, during the initial stage of the transformation [ $x_C(t) = 1$ ], the accommodation energy is found to be zero, and at the end of the transformation, the accommodation energy is at its maximum, which is similar to the variation of accommodation energy for hydrogen insertion into Nb.<sup>25</sup> The parameter “ $n$ ” in Eq. 20b determines the type of variation in accommodation energy during the progress of transformation. For example, the value of  $n$  being close to 1 corresponds to the case of linear increase in the accommodation energy. When the value of  $n$  increases further, it corresponds to the case where the accommodation energy increases quickly during the initial stages of the transformation process and then it reaches the steady state.

The chemical energy difference in Eq. 19 can be expressed as follows<sup>21</sup>

$$\Delta G_{\alpha-\beta}^{\text{chem}} = RT \left[ \frac{(C_{\beta i} - C_{\beta \alpha})}{C_{\beta \alpha}} + \frac{(C_{\alpha i} - C_{\alpha \beta})}{C_{\alpha \beta}} \right] \quad [21]$$

Rearranging Eq. 18 by using Eq. 19 and 21, one obtains

$$\Delta G_{\alpha-\beta}^i = RT \left[ \frac{C_{\beta i}}{C_{\beta \alpha}} + \frac{C_{\alpha i}}{C_{\alpha \beta}} - 2 \right] (1 - A \times P \times f[x_C(t)]) \quad [22]$$

Similar to the case of Eq. 17, the diffusion flux of  $\text{Li}^+$  ions/electrons toward the interface can be written as follows

$$j_{\text{Li}}^\beta = D_\alpha \left( \frac{\partial C_\alpha}{\partial x} \right)_{x=x_C(t)} - D_\beta \left( \frac{\partial C_\beta}{\partial x} \right)_{x=x_C(t)} \quad [23]$$

From Eq. 17, 22, and 23,  $C_{\beta i}$  can be calculated and it is given by the following expression

$$\left( \frac{C_{\beta i}}{C_{\beta \alpha}} + \frac{C_{\alpha i}}{C_{\alpha \beta}} - 2 \right) (C_{\beta i} - C_{\alpha i}) = \frac{D_\beta \left( \frac{\partial C_\beta}{\partial x} \right)_{x=x_C(t)} - D_\alpha \left( \frac{\partial C_\alpha}{\partial x} \right)_{x=x_C(t)}}{MRT \{1 - A \times P \times f[x_C(t)]\}} \quad [24]$$

When the interface mobility is very fast, i.e., ( $M \rightarrow \infty$ ),  $C_{\alpha i}$  and  $C_{\beta i}$  from Eq. 16 and 24 will be equal to the equilibrium concentrations, i.e.,  $C_{\alpha \beta}$  and  $C_{\beta \alpha}$ , respectively. In such a case, the system of equations corresponds to the case of diffusion-controlled phase transformation, which was previously modeled by Zhang et al.<sup>15</sup> When lithium diffusion in region I and lithium diffusion in  $\alpha$  phase (at region II) are neglected and when  $M \rightarrow \infty$ , the system of equations corresponds to the case of diffusion-controlled phase transformation, which was previously modeled by Srinivasan et al.<sup>14</sup> When lithium diffusion in region I, in  $\alpha$  phase at region II, and the driving force induced from the interfacial concentration difference in the  $\alpha$  phase are neglected and the coherent interface is ignored, the system of equations corresponds to the case of mixed-mode phase transformation, which was described in Ref. 16.

To perform the calculations valid for a large range of parameter values, Eq. 1-16 and 24 are now written in dimensionless form by using the procedure mentioned in Ref. 14. Thus, the system of equations in dimensionless form describes, mathematically, a nonlinear and moving boundary value problem. This differential model in this article is solved by using the numerical method of lines (MOL) in a commercial software Maple.<sup>26,27</sup> In the numerical MOL, the system of partial differential equations is converted into a system of differential-algebraic equations (DAEs). Note that the discretization is performed for the "space" variables. The resulting system of DAEs is then solved by using time-integration techniques. Details on the method of lines can be found elsewhere<sup>26,27</sup> and will not be discussed here. To check for the accuracy of the MOL, the system of equations is solved by using the numerical approach mentioned in Ref. 15. The comparison between the results obtained from the two methods indicates that they match well, which shows the accuracy of numerical MOL in solving moving boundary-type problems.

**Voltage determination.—Equilibrium potential.**—Figure 2 shows the discharge equilibrium potential vs Li content curves obtained from the galvanostatic intermittent titration technique (GITT) method using a commercial  $\text{LiFePO}_4$  electrode provided by an industry. The Li content  $x$  in  $\text{Li}_x\text{FePO}_4$  is calculated by dividing the capacity with theoretical capacity ( $x = 1$  for  $Q_d = 170$  mAh/g) of electrode. The equilibrium potential curve consists of two descending curves connected by a plateau. This plateau corresponds to the region of phase change and the two descending curves correspond to the solid solution. To use the data obtained from the GITT in the model presented in this article, an empirical relation between the equilibrium potential and the Li content  $x$  in  $\text{Li}_x\text{FePO}_4$  was obtained by a curve fitting. This equation is found to be

$$U = 3.4245 + 0.85 \times e^{[-800(x)^{1.3}]} - 17 \times e^{-(0.98)/[(x)]^{14}} \quad [25]$$

where Li content  $x$  in  $\text{LiFePO}_4$  in Eq. 25 is the ratio of the surface concentration to the maximum concentration of lithium that can be incorporated into an  $\text{FePO}_4$  lattice ( $C_i$ ). The value of  $C_i$  is calculated from GITT and Faraday's law. From Fig. 2, a close match between experimental results and the model fit can be seen. The solid-phase

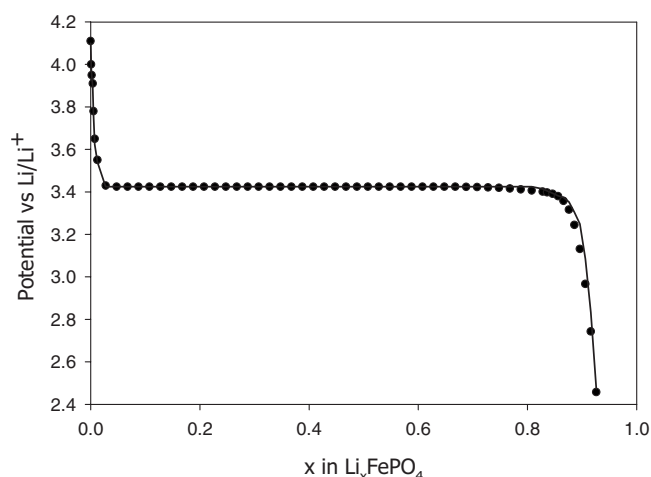


**Figure 2.** Equilibrium potential vs Li content  $x$  in  $\text{Li}_x\text{FePO}_4$  obtained from experiment and Eq. 25.

lithium concentration at the surface, obtained by solving the system of equations, is inserted into Eq. 25 and the equilibrium potential as a function of time is then calculated. From Fig. 2, the equilibrium concentration of the Li-rich phase and the Li-deficient phases was found to be  $0.85 \times 0.02119$  and  $0.027 \times 0.02119$  mol/cm<sup>3</sup>, respectively.

**Overpotential and exchange current.**—The overpotential can be calculated using following equation<sup>28</sup>

$$i = i_0 \left( \frac{(C_t - C_{\alpha s})}{C_t - \left( \frac{C_{\alpha|x=0} + C_{\alpha s}}{2} \right)} \times e^{[\alpha F \eta(t)]/RT} - \frac{C_{\alpha s}}{\left( \frac{C_{\alpha|x=0} + C_{\alpha s}}{2} \right)} \times e^{[\alpha F \eta(t)]/RT} \right) \text{ for region I} \quad [26a]$$

$$i = i_0 \left( \frac{(C_t - C_{\beta s})}{(C_t - C_{\beta \alpha})} \times e^{[\alpha F \eta(t)]/RT} - \frac{C_{\beta s}}{C_{\beta \alpha}} \times e^{[\alpha F \eta(t)]/RT} \right) \text{ for region II and region III} \quad [26b]$$

where  $i_0$  is the exchange current,  $C_{\beta s}$  is the surface concentration in the  $\beta$  phase,  $C_{\alpha s}$  is the surface concentration in the  $\alpha$  phase, and  $C_{\alpha|x=0}$  is the concentration at the central point in  $\alpha$  phase. ( $C_{\alpha i} + C_{\alpha s})/2$  is approximately equal to the equilibrium concentration. The voltage of  $\text{LiFePO}_4$  electrode is calculated by adding the overpotential to the equilibrium potential. An exchange current density value of 0.25 A/g (measured by electrochemical impedance spectroscopy using commercial  $\text{LiFePO}_4$  materials) is used for simulation.<sup>16</sup>

**Parameter estimation for  $2L_0$ ,  $\rho$ ,  $\alpha$ ,  $A$ ,  $D$ ,  $M$ , and  $n$ .**—For all the simulations, the particle size ( $2L_0$ ) was assumed to be 0.8  $\mu\text{m}$  according to scanning electron microscopy observation. The values of the density ( $\rho$ ) (3.6 g/cm<sup>3</sup>) and that of transfer coefficient ( $\alpha$ ) (0.5) were taken from Ref. 14. Because the effect of the accommodation energy on the phase transformation is not known, the value of parameter  $A$  was taken as 1. This is considered as the base case, and the value of parameter  $A$  will be decreased with the decrease in volume change (see later sections). Because the experimental determination of accurate values of diffusion coefficient and interface mobility is difficult, the values of these parameters are extracted by fitting the model to the experimental discharge curves at 20 and 10 C in Fig. 3. The end of discharge values at 20 and 10 C were



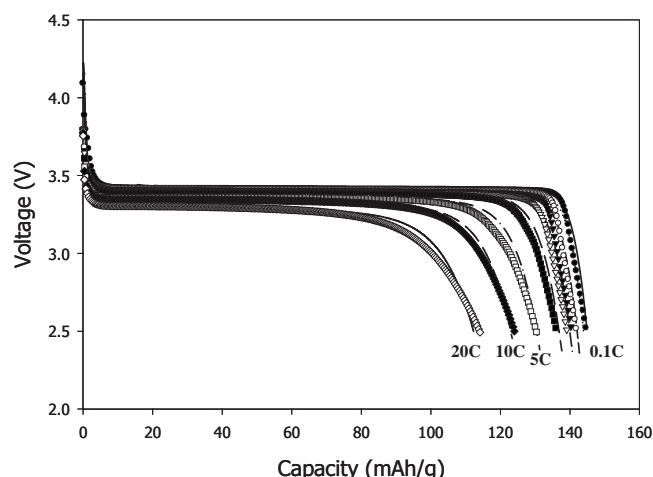


**Figure 3.** Discharge curves of a commercial  $\text{LiFePO}_4$  electrode obtained from experiment and model at 20, 10, 5, 2, 1, 0.5, 0.2, and 0.1 C (symbols: experiment; lines: model).

used to estimate the parameter  $n$ . By using this procedure, the fitted values for  $D_\beta$ ,  $M$ , and  $n$  were found to be  $3.2 \times 10^{-13} \text{ m}^2/\text{s}$ ,  $1.05 \times 10^{-10} \text{ m mol}/(\text{J s})$ , and 2.2, respectively. The diffusion coefficient in the  $\alpha$  phase is considered to be six times higher than that of the  $\beta$  phase,<sup>29</sup> and no additional efforts were made to determine the value from fitting or other approaches. The strategy adopted here for the parameter estimation and the model validation is similar to that of earlier published works.<sup>14,15,30</sup>

#### Model Validation

The model developed by Wang et al. (without consideration of lithium diffusion in the  $\alpha$  phase) was validated by predicting the discharge performance of a commercial  $\text{LiFePO}_4$  electrode having a low active material loading of  $3 \text{ mg}/\text{cm}^2$ ,<sup>16</sup> where the electrolyte resistance can be ignored. The modified model here was validated by matching not only the plateau potentials, the end of discharge values, but also the initial discharge curves of the commercial  $\text{LiFePO}_4$  electrode, which cannot be done with the model developed by Wang et al.<sup>16</sup> Figure 3 represents the voltage vs discharge capacity curves for the commercial  $\text{LiFePO}_4$  at different currents. The excellent agreement between the experimental and the modeling results at all currents is attributed to the low active material loading ( $3 \text{ mg}/\text{cm}^2$ ). In addition to this, when the interface mobility is changed to  $1.3 \times 10^{-7} \text{ m mol}/(\text{J s})$ , the model predictions (for the discharge behavior) at different currents were similar to those of the discharge behavior predicted by the shrinking core model as proposed by Zhang et al.<sup>15</sup> This behavior strongly supports the applicability of the model to a wide range of electrodes whose discharge process is either controlled by a diffusion process or the rate of phase transformation process.

Recently, Methong et al.<sup>10</sup> reported that the cation-doped nano-scale  $\text{LiFePO}_4$  (sample NC) has a higher rate capability than  $\text{LiFePO}_4$  from Aldrich chemical (sample AC) due to the extended miscibility gap, which resulted from the formation of a coherent interface between the  $\alpha$  and  $\beta$  phases. To validate the model further, here an effort was made to predict the difference in rate capability behaviors of these two samples. Particle size, solid solution limits, and equilibrium potential curves for the two samples were taken from Ref. 10. Sample NC was considered to have a coherent interface and sample AC was considered to have a semicoherent interface between  $\alpha$  and  $\beta$  phases. Because the coherent interface has a higher interface mobility than the semicoherent interface, a higher interface mobility value was used for sample NC compared to sample AC. For both of the samples, the value of the parameter  $A$  was taken as 1. This implies that the lattice strains in the samples

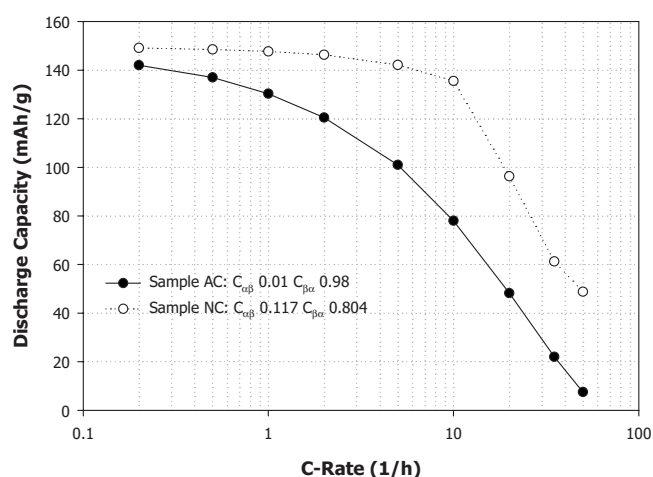


**Figure 4.** Rate capability behavior predicted from the model for samples NC and AC reported in Ref. 10. Parameters used for sample NC:  $D_\beta = 1 \times 10^{-17} \text{ m}^2/\text{s}$ ,  $M = 3 \times 10^{-11} \text{ m mol}/(\text{J s})$ ,  $A = 1$ ,  $P = 0.5$ , interface = Coherent. Parameters used for sample AC:  $D_\beta = 8 \times 10^{-16} \text{ m}^2/\text{s}$ ,  $M = 7.3 \times 10^{-12} \text{ m mol}/(\text{J s})$ ,  $A = 1$ ,  $P = 1$ , interface = semicoherent.

were high and not relieved. Figure 4 shows the rate capability behavior of two samples predicted by the model. The rate capability behavior of the two samples predicted from the model is similar to that of the experimental results reported.<sup>10</sup> The difference in rate capability observed for the two samples is due to the difference in their solid solution range and the types of interface. These results strongly validate the applicability of the model to electrode materials with different structure and properties.

#### Analysis

**Case 1: Effect of increasing the solid solution range on rate capability.**—Because the model is able to predict the rate capability behavior of two samples with different miscibility gaps, it can be used to determine the rate capability of materials with different solid solution range. The results recently reported<sup>5,10-13</sup> suggest that the doping/substitution affects the  $\alpha$  and  $\beta$  solid solutions ranges, which largely changed the rate performance of  $\text{LiFePO}_4$ . To get a broader understanding of the relation between the solid solution and the rate capability, we investigated the effects of increasing the  $\alpha$  solid solution alone, increasing the  $\beta$  solid solution alone, and increasing both  $\alpha$  and  $\beta$  solid solutions simultaneously on the discharge behavior. Because the effect of extending the  $\beta$  solid solution alone was analyzed earlier,<sup>16</sup> this study will focus on two cases, i.e., case 1: the effect of increasing the  $\alpha$  solid solution alone on the rate performance, and case 2: the effect of increasing both  $\alpha$  and  $\beta$  solid solutions simultaneously on the rate performance. The increase in the solid solution range in  $\text{LiFePO}_4$  will reduce the crystallographic mismatch due to a small concentration difference between  $C_{\alpha\beta}$  and  $C_{\beta\alpha}$ . The decrease in the crystallographic mismatch may change the nature of the interface from incoherence to semicoherence, and even to coherence. It will also change the accommodation energy, which can be captured in the model by the variation of the parameter  $A$  and  $f[x_C(t)]$  (Eq. 20a and 20b). To simplify the calculation, it is assumed that the interface maintains its state of coherence during the change in solid solution region, and that the accommodation energy decreases linearly with the decrease in concentration range [the value of parameter  $A$  was taken as the ratio of  $(C_{\beta\alpha} - C_{\alpha\beta})$  to  $(0.77 - 0.015)$ ]. Changing the solid solution range means to change the equilibrium concentration of Li-deficient and Li-rich phases. This is also evident from looking at the equilibrium potential curves of sample AC  $\text{LiFePO}_4$  and sample NC  $\text{LiFePO}_4$ .<sup>10</sup> The change in equilibrium potential curve with the change in solid solution can be modeled by changing the coefficients in Eq. 25. Throughout this

**Table I.** List of parameter values used for analysis on LiFePO<sub>4</sub> cathode materials.

Parameter	Commercial LiFePO <sub>4</sub> sample	Case 1(a)	Case 1(b)	Case 2
Length of the FePO <sub>4</sub> particle ( $2L_o$ ) ( $\mu\text{m}$ )	0.8	0.8	0.8	0.8
Density of FePO <sub>4</sub> particle ( $\rho$ ) ( $\text{g}/\text{cm}^3$ )	3.6	3.6	3.6	3.6
Li chemical diffusion coefficient in $\beta$ phase ( $D_\beta$ ) ( $\text{m}^2/\text{s}$ )	$3.2 \times 10^{-13}$	$8 \times 10^{-14}$	$8 \times 10^{-14}$	$8 \times 10^{-17}$ – $8 \times 10^{-14}$
Li chemical diffusion coefficient in $\alpha$ phase ( $D_\alpha$ ) ( $\text{m}^2/\text{s}$ )	$6 \times D_\beta$	$6 \times D_\beta$	$6 \times D_\beta$	$6 \times D_\beta$
Interface mobility ( $M$ ) ( $\text{m mol}/(\text{J s})$ )	$1.05 \times 10^{-10}$	$6.3 \times 10^{-12}$	$6.3 \times 10^{-12}$	$1.3 \times 10^{-12}$ – $1.3 \times 10^{-10}$
Dimensionless equilibrium concentration of Li-deficient phase ( $C_{\alpha\beta}/C_l$ )	0.027	0.015–0.4	0.015–0.35	0.015
Dimensionless equilibrium concentration of Li-rich phase ( $C_{\beta\alpha}/C_l$ )	0.85	0.77	0.77–0.45	0.77
Exchange current ( $i_o$ ) (A/g)	0.25	0.1	0.1	0.1
Accommodation energy factor ( $A$ )	1.0	1.0–0.49	1–0.13	1.0
Proportionality factor ( $P$ )	1.0	1.0	1.0	1.0
$n$	2.2	2.2	2.2	2.2
$C_l$ ( $\text{mol}/\text{cm}^3$ )	0.02119	0.02044	0.02044	0.02044

analysis, the parameters other than  $C_{\alpha\beta}$ ,  $C_{\beta\alpha}$ , and  $A$  were kept constant (see Table I). Also, the maximum lithium that can be incorporated into the FePO<sub>4</sub> lattice ( $C_l$ ) was assumed to remain constant with the doping/substitution.

**Case 1(a): Effect of extending the  $\alpha$  solid solution.**— The effect of increasing the  $\alpha$  solid solution range of LiFePO<sub>4</sub> on the rate performance was determined by increasing  $C_{\alpha\beta}$  from 0.015 to 0.4 (while keeping  $C_{\beta\alpha}$  constant), i.e., from a phase change material to a large solid solution material. Figure 5 shows the equilibrium potential curves obtained from Eq. 25, which correspond to  $C_{\alpha\beta}$  values of 0.015, 0.1, 0.15, 0.2, 0.25, 0.30, 0.35, and 0.4, respectively. The discharge behaviors of LiFePO<sub>4</sub> with different  $\alpha$  solid solution limits at current densities of 5, 10, and 20 C were simulated and the rate performance of LiFePO<sub>4</sub> is shown in Fig. 6 and 7. The discharge capacity of LiFePO<sub>4</sub> seems to increase monotonically with the increase in  $\alpha$  solid solution irrespective of discharge current used. However, at lower currents up to 5 C (Fig. 6), the discharge capacity

reaches the maximum value with a small increase in  $C_{\alpha\beta}$  and remains constant with a further increase in  $C_{\alpha\beta}$ . At higher currents such as 20 C (Fig. 7), a constant increase in the discharge capacity is

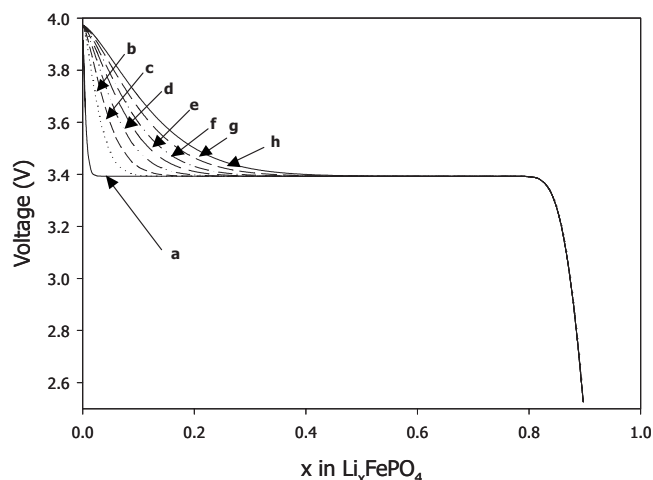


**Figure 5.** Equilibrium potential curves (obtained from Eq. 25 with different coefficients) for LiFePO<sub>4</sub> with different  $\alpha$  solid solution range (different  $C_{\alpha\beta}$  and  $C_{\beta\alpha} = 0.77$ ) as a function of Li content in FePO<sub>4</sub> during discharge process ( $C_{\alpha\beta}$  = a: 0.015, b: 0.1, c: 0.15, d: 0.2, e: 0.25, f: 0.3, g: 0.35, h: 0.4).

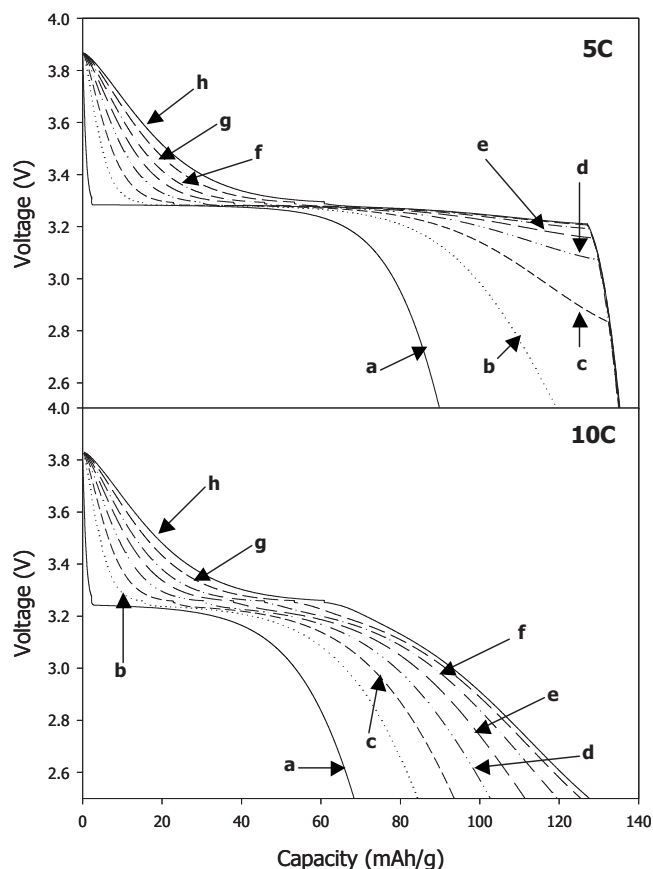


**Figure 6.** Discharge curves of LiFePO<sub>4</sub> with different  $\alpha$  solid solution limits ( $C_{\alpha\beta}$  = a: 0.015, b: 0.1, c: 0.15, d: 0.2, e: 0.25, f: 0.3, g: 0.35, h: 0.4) at 5 and 10 C.

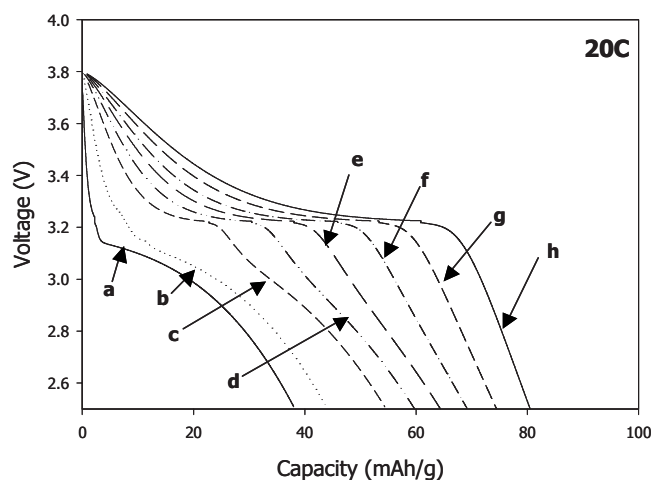


**Figure 7.** Discharge curves of  $\text{LiFePO}_4$  with different  $\alpha$  solid solution limits ( $C_{\alpha\beta}$  = a: 0.015, b: 0.1, c: 0.15, d: 0.2, e: 0.25, f: 0.3, g: 0.35, h: 0.4) at 20 C.

observed with the increase in  $C_{\alpha\beta}$ . From these results, it can be suggested that the cathode materials with higher  $\alpha$  solid solution exhibit a higher rate capability than the materials with a lower  $\alpha$  solid solution, provided that the diffusion coefficient and interface mobility are not lowered with the increase in  $\alpha$  solid solution.

*Case 1(b): Effect of extending the  $\alpha$ ,  $\beta$  solid solutions simultaneously.*—The effect of increasing  $\alpha$  and  $\beta$  solid solutions of  $\text{LiFePO}_4$  simultaneously on the rate performance was achieved by increasing  $C_{\alpha\beta}$  from 0.015 to 0.35 while changing  $C_{\beta\alpha}$  from 0.77 to 0.45, i.e., from a phase change material to a solid solution material. Figure 8 shows the equilibrium potential curves obtained from Eq. 25, with different values of  $C_{\alpha\beta}$  corresponding to 0.015, 0.1, 0.15, 0.2, 0.25, 0.30, 0.35, and  $C_{\beta\alpha}$  corresponding to 0.77, 0.7, 0.65, 0.6, 0.55, 0.5, and 0.45, respectively. Figures 9 and 10 show the discharge behavior of  $\text{LiFePO}_4$  with different  $\alpha$  and  $\beta$  solid solution limits at different current densities (0.1, 10, and 20 C). The variation of discharge capacity at different C-rates with solid solution range is summarized in Fig. 11a. At all the currents, the discharge capacity reaches the maximum value with a small increase in the solid solution region and remains constant with a further increase. From these results, it seems that increasing both the solid solutions simulta-

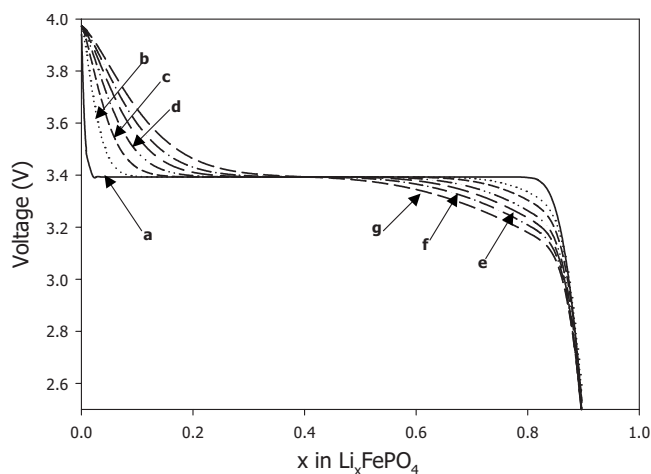


**Figure 8.** Equilibrium potential curves (obtained from Eq. 25 with different coefficients) for  $\text{LiFePO}_4$  with different  $\alpha$  and  $\beta$  solid solution ranges as a function of Li content in  $\text{FePO}_4$  during discharge process ( $C_{\alpha\beta}$  and  $C_{\beta\alpha}$ : a = 0.015 and 0.77, b = 0.1 and 0.7, c = 0.15 and 0.65, d = 0.2 and 0.6, e = 0.25 and 0.55, f = 0.3 and 0.5, g = 0.35 and 0.45).

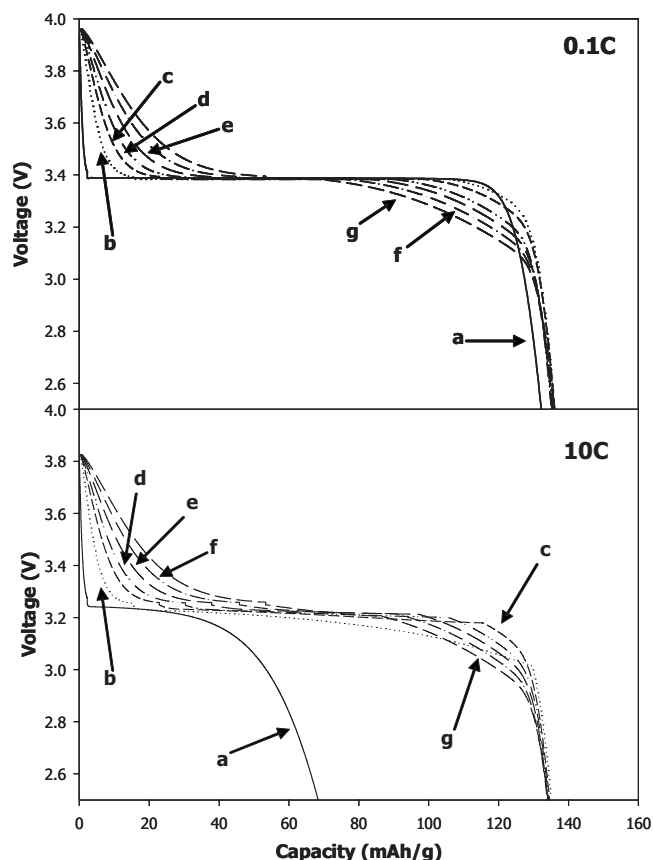


**Figure 9.** Discharge curves of  $\text{LiFePO}_4$  with different  $\alpha$  and  $\beta$  solid solution limits ( $C_{\alpha\beta}$  and  $C_{\beta\alpha}$ : a = 0.015 and 0.77, b = 0.1 and 0.7, c = 0.15 and 0.65, d = 0.2 and 0.6, e = 0.25 and 0.55, f = 0.3 and 0.5, g = 0.35 and 0.45) at 0.1 and 10 C.

neously is more beneficial than increasing one of the solid solutions, as the former one leads to a higher rate capability. However, when the diffusion coefficient in the  $\beta$  phase was lowered by 2 orders of

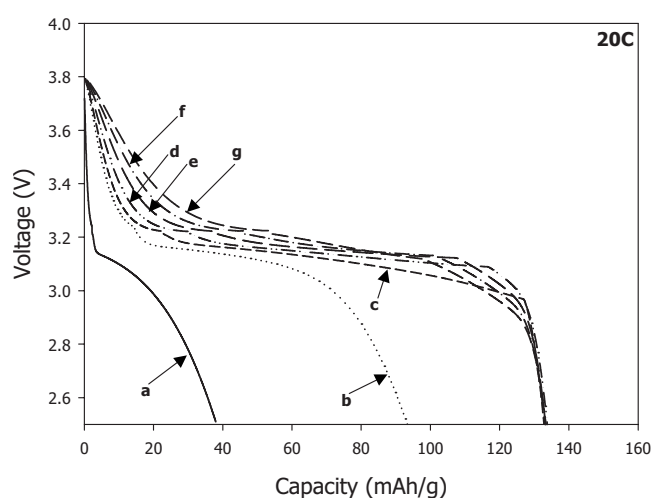


**Figure 10.** Discharge curves of  $\text{LiFePO}_4$  with different  $\alpha$  and  $\beta$  solid solution limits ( $C_{\alpha\beta}$  and  $C_{\beta\alpha}$ : a = 0.015 and 0.77, b = 0.1 and 0.7, c = 0.15 and 0.65, d = 0.2 and 0.6, e = 0.25 and 0.55, f = 0.3 and 0.5, g = 0.35 and 0.45) at 20 C.

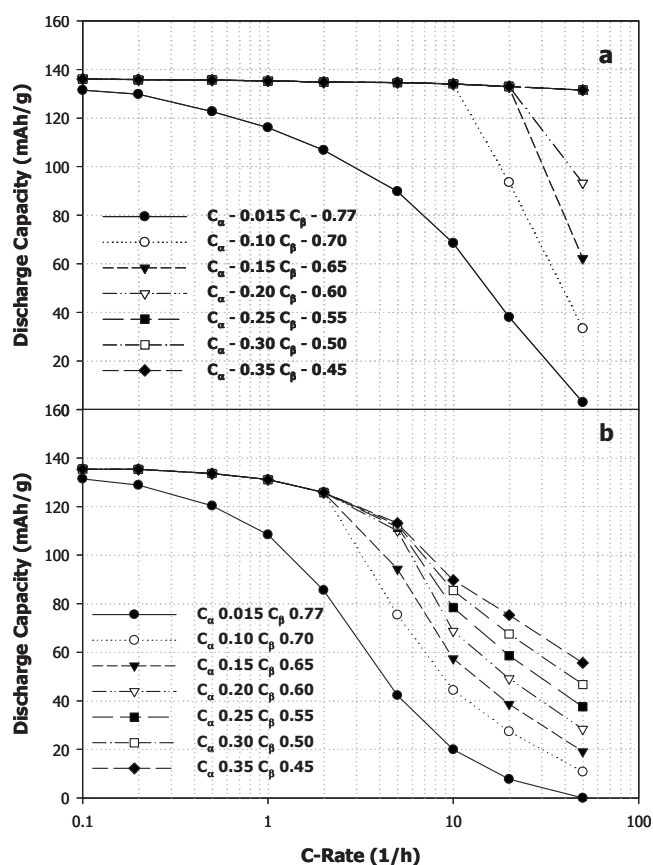


**Figure 11.** Effect of increasing  $\alpha$  and  $\beta$  solid solutions on a rate capability of  $\text{LiFePO}_4$  with a diffusion coefficient ( $D_\beta$ ) of a:  $8 \times 10^{-14} \text{ m}^2/\text{s}$ , b:  $8 \times 10^{-16} \text{ m}^2/\text{s}$ .

magnitude ( $8 \times 10^{-16} \text{ m}^2/\text{s}$ ), extending the solid solution range was found to enhance rate performance at low discharge rates as well as at high discharge rates (Fig. 11b).

**Case 2: Effect of particle size on rate capability.**— Apart from increasing the electronic conductivity and the miscibility gap, another technique widely used to increase the rate capability of  $\text{LiFePO}_4$  is to reduce the particle size to nanometers. Recently, Delacourt et al.<sup>31</sup> have shown that a high rate capability can be achieved

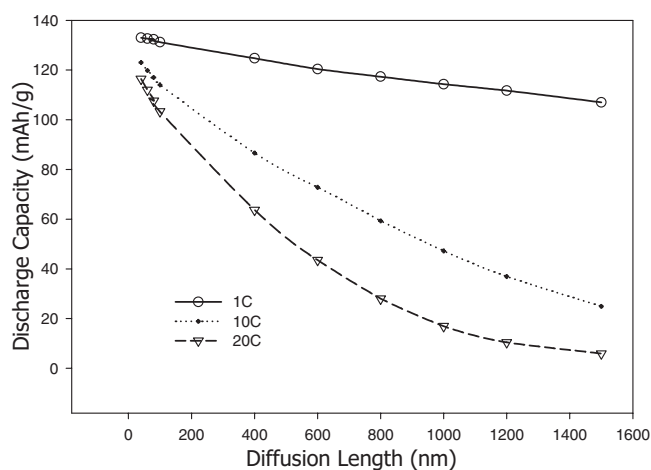


**Figure 12.** Effect of particle radius on discharge capacity of  $\text{LiFePO}_4$  at different currents [ $D_\beta = 8 \times 10^{-15} \text{ m}^2/\text{s}$ ,  $M = 6.3 \times 10^{-12} \text{ m mol}/(\text{J s})$ ].

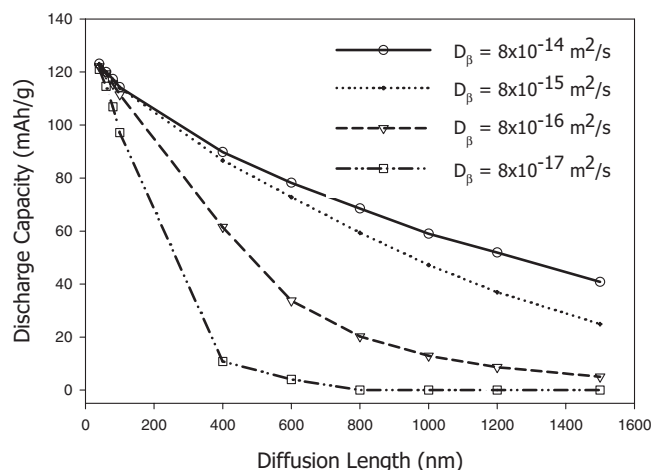


**Figure 13.** Effect of diffusion length on discharge capacity of  $\text{LiFePO}_4$  at 10 C with different diffusion capabilities [ $M = 6.3 \times 10^{-12} \text{ m mol}/(\text{J s})$ ].

for  $\text{LiFePO}_4$  without carbon coating by reducing the particle size to 140 nm. From experimental results and a simple theoretical model, it was also concluded that the electrode resistance for  $\text{LiFePO}_4$ -based cathode materials depends only on mean particle size.<sup>32</sup> In this study, an effort was made to determine the influence of particle size on the rate capability of  $\text{LiFePO}_4$  from the model. This was done by changing the  $\text{Li}^+$ -ion diffusion length from 1.5  $\mu\text{m}$  to 40 nm, while keeping all the other parameters constant (Table I). Figure 12 shows the discharge capacity of  $\text{LiFePO}_4$  at 1, 10, and 20 C as a function of diffusion length. As shown in Fig. 12, the discharge capacity at 1 C increases linearly with the decrease in diffusion length, which is in agreement with the recently reported results.<sup>32</sup> Contrary to the behavior observed at 1 C, discharge capacity at high currents (10 and 20 C) increased greatly with the decrease in diffusion length. These results imply that it is possible to attain a high rate capability for  $\text{LiFePO}_4$  by reducing the size to the order of the nanoscale. Similarly, a high rate capability can be obtained for materials with a lower chemical diffusion (Figure 13) or a lower interface mobility (Fig. 14) by reducing the diffusion length.

## Conclusions

A discharge model that involves two phases for phase transformation electrode was developed based on the theory of mixed-mode phase transformation. The model was validated by fitting the dis-

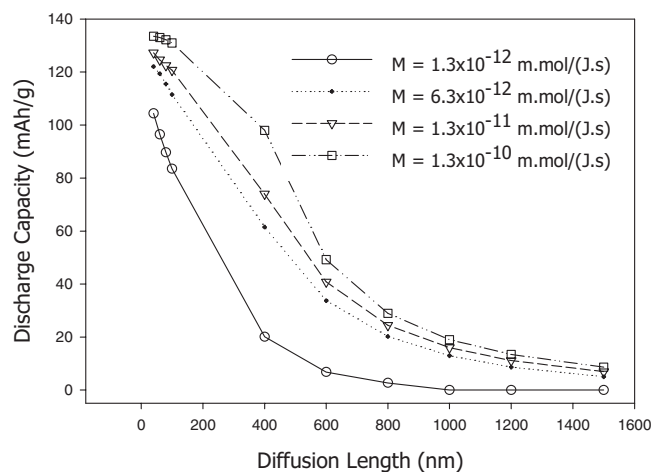


**Figure 14.** Effect of diffusion length on discharge capacity of  $\text{LiFePO}_4$  at 10 C with different interface mobilities ( $D_\beta = 8 \times 10^{-16} \text{ m}^2/\text{s}$ ).



charge behavior of a commercial  $\text{LiFePO}_4$  electrode with low active material loading obtained from industry. The model was also validated by predicting the rate capability behavior of cation-doped nanoscale  $\text{LiFePO}_4$  and conventional  $\text{LiFePO}_4$ , which differ in miscibility gap and interface structure.

The phase transformation electrodes with a wide solid solution exhibit a high rate capability except when the diffusion coefficients are very low. Increasing either the  $\alpha$  solid solution or increasing both  $\alpha$  and  $\beta$  solid solutions will increase the rate capability of the electrodes; however, the latter one has a higher impact on rate capability. Apart from increasing the miscibility gap, the rate capability of the phase transformation electrode materials can be improved by reducing the  $\text{Li}^+$ -ion diffusion length (particle size) to nanometers, though the rate of the phase transformation and chemical diffusion are low. Finally, the model developed here is applicable for electrode materials with different interface structures (coherent, semicoherent, and incoherent), different rate-controlling processes (diffusion, interface reaction, and mixed), and different solid solution ranges. We hope that the availability of such a general mathematical model will help in the development of new materials with better rate capability.

### Acknowledgments

This work was supported by the U.S. Army Communications Electronics Command under contract no. W909MY-06-C-0040. We are grateful to the Center for Manufacturing Research at Tennessee Technological University for their partial financial support during a period of this work.

University of Maryland assisted in meeting the publication costs of this article.

### List of Symbols

$A$	accommodation energy factor
$C_\alpha$	lithium concentration in $\alpha$ phase, $\text{mol}/\text{m}^3$
$C_\beta$	lithium concentration in $\beta$ phase, $\text{mol}/\text{m}^3$
$C_{\alpha\beta}$	equilibrium lithium concentration in $\alpha$ phase at the interface, $\text{mol}/\text{m}^3$
$C_{\beta\alpha}$	equilibrium lithium concentration in $\beta$ phase at the interface, $\text{mol}/\text{m}^3$
$C_{\alpha i}$	real lithium concentration in $\alpha$ phase at the interface, $\text{mol}/\text{m}^3$
$C_{\beta i}$	real lithium concentration in $\beta$ phase at the interface, $\text{mol}/\text{m}^3$
$C_{\alpha s}$	lithium concentration in $\alpha$ phase at the surface, $\text{mol}/\text{m}^3$
$C_{\beta s}$	lithium concentration in $\beta$ phase at the surface, $\text{mol}/\text{m}^3$
$C_t$	maximum lithium concentration in $\text{FePO}_4/\text{LiFePO}_4$ lattice, $\text{mol}/\text{m}^3$
$D_\alpha$	mixed diffusion coefficient in the $\alpha$ phase, $\text{m}^2/\text{s}$
$D_\beta$	mixed diffusion coefficient in the $\beta$ phase, $\text{m}^2/\text{s}$
$F$	Faraday's constant, $96,487 \text{ C/mol}$
$i$	discharge current, $\text{A}/\text{m}^2$
$i_0$	exchange current, $\text{A}/\text{m}^2$
$j_{\text{Li}}^i$	flux of $\text{Li}^+$ ions across the interface, $\text{mol}/(\text{m}^2 \text{ s})$
$j_{\text{Li}}^b$	flux of $\text{Li}^+$ ions towards the interface, $\text{mol}/(\text{m}^2 \text{ s})$
$M$	interface mobility, $\text{m}/(\text{mol}/\text{Js})$
$n$	exponential term
$P$	proportionality factor
$R$	gas constant, $8.3145 \text{ J/mol K}$

$t$	time, s
$T$	temperature, K
$x$	axial position in the particle, m
$x_0$	total $\text{Li}^+$ -ion diffusion length in the particle, m
$x_C(t)$	position of the phase boundary, m
$\Delta G_{\alpha\beta}^i$	driving force for the phase transformation, J/mol
$\Delta G_{\alpha\beta}^{\text{chem}}$	chemical free energy, J/mol
$\Delta G_{\alpha\beta}^{\text{elastic}}$	elastic accommodation energy, J/mol
$\Delta G_{\alpha\beta}^{\text{plastic}}$	plastic accommodation energy, J/mol
$\Delta G_{\alpha\beta}^{\text{surface}}$	free energy resulting from free surfaces, J/mol
$\eta(t)$	overpotential, V
$\rho$	density of $\text{LiFePO}_4$ , $\text{g}/\text{m}^3$

### References

- H. Huang, S.-C. Yin, and L. F. Nazar, *Electrochem. Solid-State Lett.*, **4**, A170 (2001).
- S. Yang, Y. Song, P. Y. Zavalij, and M. S. Whittingham, *Electrochem. Commun.*, **4**, 239 (2002).
- S.-Y. Chung, J. T. Blocking, and Y.-M. Chiang, *Nat. Mater.*, **1**, 123 (2002).
- C. Wang and J. Hong, *Electrochem. Solid-State Lett.*, **10**, A65 (2007).
- Y.-M. Chiang, N. Meethong, H.-Y. S. Huang, W. C. Carter, S. Chang, A. Hsiao, and A. S. Gozdz, presented at The Electrochemical Society Meeting, Cancun, Nov. 2006.
- M. M. Doeff, Y. Hu, F. McLarnon, and F. Kostecki, *Electrochem. Solid-State Lett.*, **6**, A207 (2003).
- P. S. Herle, B. Ellis, N. Coombs, and L. F. Nazar, *Nat. Mater.*, **3**, 147 (2004).
- C. R. Sides, F. Croce, V. Y. Young, C. R. Martin, and B. Scrosati, *Electrochem. Solid-State Lett.*, **8**, A484 (2005).
- D.-H. Kim and J. Kim, *Electrochem. Solid-State Lett.*, **9**, A439 (2006).
- N. Meethong, H.-Y. S. Huang, S. A. Speakman, W. C. Carter, and Y.-M. Chiang, *Adv. Funct. Mater.*, **17**, 1115 (2007).
- N. Meethong, H.-Y. S. Huang, S. A. Speakman, W. C. Carter, and Y.-M. Chiang, *Electrochem. Solid-State Lett.*, **10**, A134 (2007).
- T. Nakamura, K. Sakumoto, S. Seki, Y. Kobayashi, M. Tabuchi, and Y. Yamada, *J. Electrochem. Soc.*, **154**, A1118 (2007).
- T. Nakamura, K. Sakumoto, M. Okamoto, S. Seki, Y. Kobayashi, T. Takeuchi, M. Tabuchi, and Y. Yamada, *J. Power Sources*, **174**, 435 (2007).
- V. Srinivasan and J. Newman, *J. Electrochem. Soc.*, **151**, A1517 (2004).
- Q. Zhang and R. E. White, *J. Electrochem. Soc.*, **154**, A587 (2007).
- C. Wang, U. Kasavajula, and P. E. Arce, *J. Phys. Chem. C*, **111**, 16656 (2007).
- J. Sietsma and S. V. D. Zwaag, *Acta Mater.*, **52**, 4143 (2004).
- F. V. Nolfi, P. G. Shewman, and J. S. Foster, *Trans. Metall. Soc. AIME*, **245**, 1427 (1969).
- W. U. Ruiheng, R. Xueyu, H. Zhang, and T. Y. Hsu, *J. Mater. Sci. Technol.*, **20**, 561 (2004).
- J. Sietsma, M. G. Meozzi, S. M. C. Bohemen, and S. V. D. Zwaag, *Int. J. Mater. Res.*, **97**, 356 (2006).
- D. A. Porter and K. E. Easterling, *Phase Transformations in Metals and Alloys*, 2nd ed., Chapman & Hall, London (1992).
- Y. C. Liu, F. Sommer, and E. J. Mittemeijer, *Acta Mater.*, **52**, 2549 (2004).
- B. W. Leitch and S.-Q. Shi, *Modell. Simul. Mater. Sci. Eng.*, **4**, 281 (1996).
- G. Chen, X. Song, and T. J. Richardson, *Electrochem. Solid-State Lett.*, **9**, A295 (2006).
- R. J. Balasubramanian, *J. Alloys Compd.*, **253**, 203 (1997).
- U. Nowak, *Appl. Numer. Math.*, **20**, 129 (1996).
- W. Zhang, *Appl. Numer. Math.*, **20**, 235 (1996).
- A. J. Bard and L. R. Faulkner, *Electrochemical Methods*, 2nd ed., p. 99, John Wiley & Sons, Inc., New York (2004).
- Annual Progress Report on Energy Storage Research and Development, Freedom Car and Vehicle Technologies Program (2005).
- K. Striabel, J. Shim, V. Srinivasan, and J. Newman, *J. Electrochem. Soc.*, **152**, A664 (2005).
- C. Delacourt, P. Poizot, S. Levasseur, and C. Masquelier, *Electrochem. Solid-State Lett.*, **9**, A352 (2006).
- M. Gaberscek, R. Dominko, and J. Jamnik, *Electrochem. Commun.*, **9**, 2778 (2007).